ADVANCED ENERGY MATERIALS
www.advenergymat.de

Rational Design of Coating Ions via Advantageous Surface Reconstruction in High-Nickel Layered Oxide Cathodes for Lithium-Ion Batteries

*Youngjin Kim, Hyoju Park, Kihyun Shin, Graeme Henkelman, Jamie H. Warner, and Arumugam Manthiram**

The implementation of high-nickel layered oxide cathodes in lithium-ion batteries is hampered by the inherent issues of formation of NiO-like rock-salt phase as well as residual lithium (e.g., LiOH, $LiHCO_3$, and Li_2CO_3) on the surface. To overcome the challenges, here a rational strategy is presented of interdiffusion-based surface reconstruction via dry coating and the design principles for identifying the optimum coating ions on a $LiNi_{0.91}Mn_{0.03}Co_{0.06}O_2$ (NMC91) cathode. Notably, the combined approach of theoretical screening, which involves the consideration of superexchange interactions among different oxidation states and density functional theory calculations, along with experimental analyses, which involve the characterization of the decrease in Ni content and residual lithium on the surface of NMC91, demonstrate the effective reduction in rock-salt phase and residual lithium. Among the four ions investigated (Al, Co, Fe, and Ti), cobalt-coated NMC91 is the most effective at reducing the rock-salt phase and residual lithium by successfully reconstructing the surface of NMC91 and exhibits an excellent capacity retention of 85% in a full cell after 300 cycles at 30 °C.

1. Introduction

The global automobile market is currently at the cusp of a paradigm shift from reliance on internal combustion engine vehicles (ICEVs) to electric vehicles (EVs). Consequently, the soaring demand for large-scale energy storage devices is anticipated to fuel the growth of the global energy storage market. Lithium-ion batteries (LIBs), thus far, maintain a dominant position in the global energy storage market through cutting-edge innovation over various candidates.[1] With LIBs, however, many EV manufacturers have been struggling to achieve competitive cost over the ICEV rivals.[2] In their efforts to reach price parity with ICEVs, EV manufacturers have sought to considerably improve the cathode materials, which is the most expensive component in LIBs. High-nickel layered oxides (Ni ≥ 80%), such as $LiNi_xMn_yCo_{1-x-y}O_2$ (NMC) and $LiNi_xCo_yAl_{1-x-y}O_2$ (NCA), are definitely at the forefront among various cathode material contenders due to their higher energy density and lower cost.[3]

The high-Ni layered oxides, however, are yet to achieve long-term cycling and thermal stability due to two inherent issues owing to the chemical instability of Ni^{3+}. One of the undesirable issues is the phase transition from layered to NiO-like rock-salt structure that takes place on the surface of the cathode due to the formation of Ni^{2+} with increasing Ni content in the layered oxide. Synthesis at high temperature,[4] storage in air,[5] and repeated electrochemical cycling[6] of high-Ni cathode materials cause a layered-to-rock-salt phase transition, inhibiting lithium-ion transport from the cathode surface to its bulk. In addition, residual lithium compounds containing LiOH, $LiHCO_3$, and Li_2CO_3 can be formed on the surface of high-Ni cathode from its reaction with moisture and carbon dioxide in air.[7] These residual lithium compounds cause detrimental issues, namely gas evolution during battery operation and slurry gelation during battery manufacturing.[8] While the current state-of-the-art high-Ni layered oxide cathode materials are a potential long-term solution for EVs, these inherent challenges must be addressed for their practical implementation.

Substantial surface modification through coating and/or doping became essential in overcoming the challenges throughout the history of cathode materials for commercial LIBs. In particular, the strategy of surface coating has been extensively applied to most of cathode materials, including $LiCoO_2$ to effectively suppress their side reaction with the electrolyte, leading to improved electrochemical performance.[9] To realize commercially applicable high-Ni layered oxide cathodes for high-energy-density LIBs, there is an urgent demand from academia and industry for the design of appropriate coating materials capable of addressing both the issues of rock-salt phase and residual lithium formation

Y. Kim, H. Park, J. H. Warner, A. Manthiram
Department of Mechanical Engineering and Texas Materials Institute
The University of Texas at Austin
Austin, TX 78712, USA
E-mail: manth@austin.utexas.edu
K. Shin, G. Henkelman
Department of Chemistry and the Oden Institute for Computational Engineering and Science
The University of Texas at Austin
Austin, TX 78712, USA

The ORCID identification number(s) for the author(s) of this article can be found under https://doi.org/10.1002/aenm.202101112.

DOI: 10.1002/aenm.202101112

© 2021 Wiley-VCH GmbH

on the surface of the material. This requires a comprehensive understanding of the surface chemistry and affinity of the coating ions in high-Ni oxides to design an effective strategy.

Interdiffusion-based beneficial surface reconstruction via coating on high-Ni cathode surface can effectively address both issues. For example, coating precursor reacts with the residual lithium on the surface of the high-Ni oxide material upon annealing to reduce the residual lithium remaining on the surface. In addition, it was discovered that interdiffusion of transition-metal (TM) cations occur between the coating precursors (which becomes an oxide upon annealing) and the high-Ni layered oxide, lowering the concentration of Ni at the surface.[10] Such a surface modification suggests that applying a coating precursor of an appropriate metal can serve to not only reduce the residual lithium compounds but also decrease the Ni concentration at the surface via the interdiffusion phenomenon, reducing the rock-salt phase formation. Also, as the coating precursors must be compatible with high-Ni layered oxides during the dry coating process, metal hydroxides or oxides would be the appropriate candidates. Based on this, it would be immensely valuable to investigate the efficacy of various metal hydroxides or oxides for the dry coating method on addressing both the issues of rock-salt phase and residual lithium formation on the surface of high-Ni oxides and identify the optimum coating ion.

Herein, for the first time, we provide new insights into the rational strategy of interdiffusion-based favorable surface reconstruction via dry coating to mitigate both the issues of rock-salt phase formation and residual lithium contents on the surface of NMC91 and the optimum coating ion for this strategy. Among the various metals, Al and Co were screened as the optimum candidates for experimental investigation based on theoretical considerations, including the superexchange stability of the coating ions supported by density functional theory (DFT) calculations. In addition to Al and Co, Ti and Fe, which were determined unfavorable, were also investigated to verify the rationality of the screening process. Empirically, the effect of applying the metal hydroxides or oxides of Al, Ti, Fe, and Co as the coating material was thoroughly explored with state-of-the-art surface and bulk characterization techniques, such as high-resolution scanning transmission electron microscopy (HR-STEM) and time-of-flight secondary-ion mass spectrometry (ToF-SIMS) analyses, which offer critical information regarding the surface properties of the uncoated and coated NMC91 materials. Both Al- and Co-coated NMC91 demonstrate significantly reduced rock-salt phase and residual lithium content, but the cobalt-coated NMC91 exhibit superior cycling performance and thus was determined as the optimum coating ion. Ti and Fe, on the other hand, were not as effective as Al or Co in reducing the rock-salt phase or the residual lithium content and lead to worse electrochemical performance compared to the uncoated NMC91. Contrasting results of Al and Co coating compared to Ti and Fe coating verified the rationality of the screening process. Finally, we expect our design principles presented herein to provide a step forward to mitigating the inherent challenges of high-Ni layered oxides and lead to the development of commercial high-Ni layered oxide cathode materials.

2. Results and Discussion

2.1. Devising an Effective Surface Modification Strategy: Interdiffusion-Based Surface Reconstruction via Dry Coating Process

As mentioned above, both the residual lithium formation and layered-to-rock-salt phase transition on the surface of high-Ni layered oxides stem from a key feature, the instability of Ni^{3+}, which is best demonstrated by $LiNiO_2$ (LNO). Despite the extensive investigations on the synthesis of stoichiometric high-Ni layered oxide, such as LNO, under strong oxidation environment over several decades, the stoichiometric LNO phase is yet to be reported. Instead, the off-stoichiometric $Li_{1-x}Ni_{1+x}O_2$ forms as described below during the synthesis of LNO:[4a,b,11]

$$\mathrm{LiNiO_2} \rightarrow 1/(1+x)\,\mathrm{Li}_{1-x}\mathrm{Ni}_{1+x}\mathrm{O}_2 + x/(1+x)\,\mathrm{Li_2O} + x/2(1+x)\,\mathrm{O_2} \qquad (1)$$

The off-stoichiometric $Li_{1-x}Ni_{1+x}O_2$ is composed of two phases, the off-stoichiometric layered phase ($x < 0.38$) in the bulk and the NiO-like rock-salt phase ($x > 0.38$) on the surface.[4a] Some of the Ni exists as Ni^{2+} and migrates to the lithium layer in $Li_{1-x}Ni_{1+x}O_2$ due to the relative stability of Ni^{2+} over Ni^{3+} in the layered oxide structure and the migration is accompanied by the extraction of lithium and release of oxygen from the lattice to maintain charge neutrality via Equation (1).[4a,b,12] This reaction takes place at the surface of the $Li_{1-x}Ni_{1+x}O_2$ where oxygen can be easily released and results in the formation of lithium oxide (Li_2O). In addition, residual lithium forms on the surface of LNO due to Ni^{3+} instability under the presence of moisture and carbon dioxide in air.[13] The formation mechanism of residual lithium on the LNO surface is described below in Equations (2) and (3):

$$\mathrm{LiNiO_2} + (y/2)\,\mathrm{H_2O} \rightarrow \mathrm{Li}_{1-y}\mathrm{NiO}_{2-(y/2)} + y\mathrm{LiOH} \qquad (2)$$

$$\mathrm{LiNiO_2} + (z/2)\,\mathrm{CO_2} \rightarrow \mathrm{Li}_{1-z}\mathrm{NiO}_{2-z} + (z/2)\,\mathrm{Li_2CO_3} + (z/4)\,\mathrm{O_2} \qquad (3)$$

From the formation mechanisms of both the rock-salt phase and the residual lithium, it can be deduced that in essence, both are surface phenomena that involves reduction of Ni^{3+} to Ni^{2+} accompanied by the extraction of lithium and release of oxygen (i.e., increase in lithium deficiency and Ni^{2+} content). Additionally, Li_2O in Equation (1) is spontaneously converted to LiOH and Li_2CO_3 in air ($\Delta G < 0$) and adds to the residual lithium concentration. Thus, the key to mitigating the two issues would be to suppress the reduction of relatively unstable Ni^{3+} to the more stable Ni^{2+} at the surface. High-Ni NMC and NCA are known to suffer from the same issues as well, indicating that those issues are aggravated as the Ni content increases in the layered oxide.[6e] Hence, we aimed to devise a surface modification strategy that can address both the issues of rock-salt phase and residual lithium formation by suppressing the formation of Ni^{2+} at the surface of high-Ni layered oxides.

Figure 1a illustrates our intended strategy behind simultaneous reduction of the rock-salt phase formation and the residual lithium content at the surface of a high-Ni layered oxide. Unfortunately, this cannot be achieved through conventional methods. As illustrated in Figure 1b, with a typical dry

© 2021 Wiley-VCH GmbH

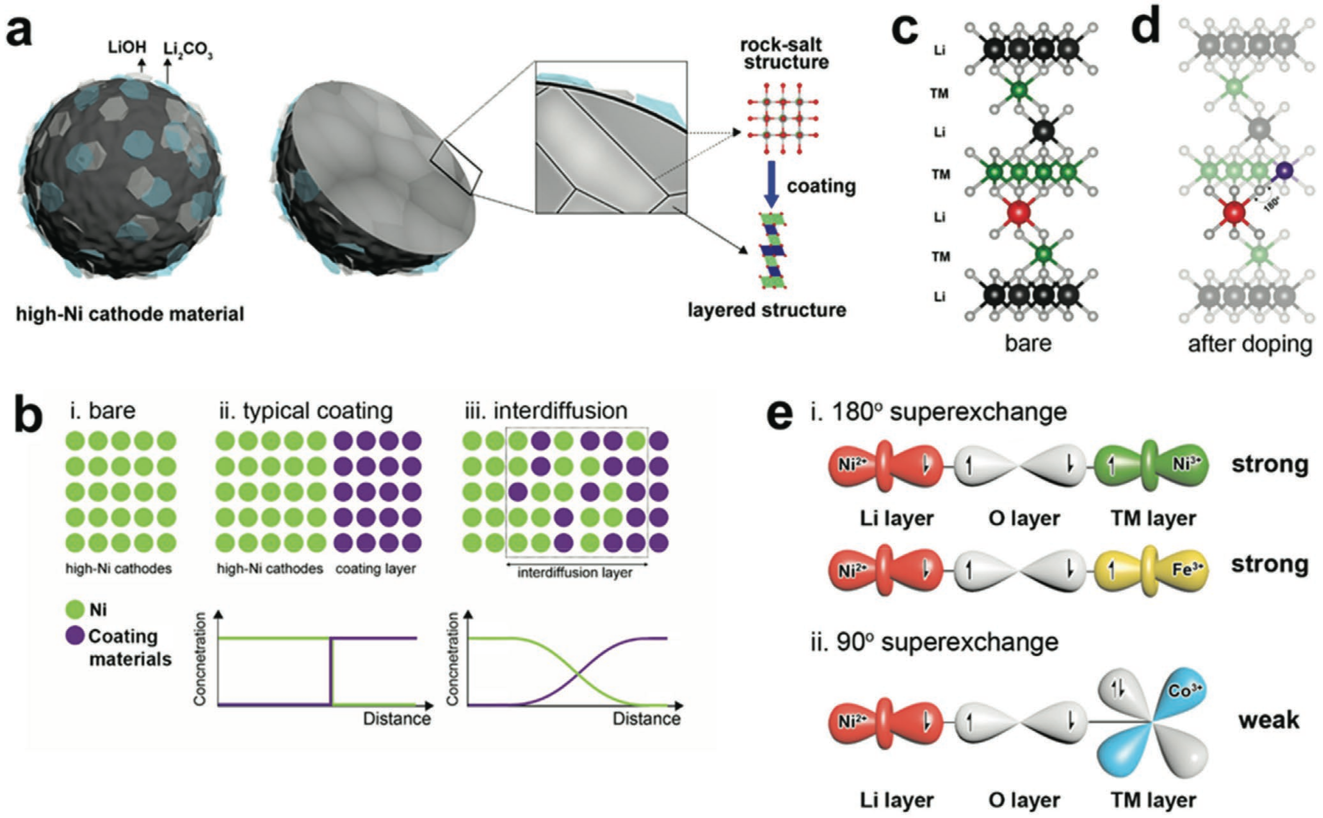

Figure 1. Schematic illustration of the intrinsic issues and characteristics of high-Ni layered oxides. a) Residual lithium species (LiOH and Li_2CO_3) on the surface of high Ni-layered oxides and the structural change achieved by our proposed surface reconstruction of high-Ni layered oxides, b) elemental distribution characteristics on the surface of high-Ni layered oxides: (i) untreated; (ii) typical coating; and (iii) interdiffusion, Li/Ni mixing in high-Ni layered oxides c) before and d) after interdiffusion, and e) superexchange interaction of Ni^{2+}-O^{2-}-M: (i) 180° (M: Ni^{3+} and Fe^{3+}) and (ii) 90° (M: Co^{3+}) superexchange. Electron configuration: Ni^{2+} ($t_{2g}^6 d_{z2}^1 d_{x2-y2}^1$), Ni^{3+} ($t_{2g}^6 d_{z2}^1 d_{x2-y2}^0$), Fe^{3+} ($t_{2g}^3 d_{z2}^1 d_{x2-y2}^1$), and Co^{3+} (t_{2g}^6).

coating process, the coating material reacts with the residual lithium species to form a new layer at the surface of a high-Ni layered oxide, in effect reducing the residual lithium concentration. However, this does not effectively suppress the issue of rock-salt phase formation at the surface of the high-Ni layered oxide. Elemental doping, on the other hand, is able to suppress the layered-to-rock-salt phase transition, but the doping effect on the surface is relatively minor due to the dopant being homogeneously diffused throughout the bulk of the high-Ni layered oxide material.[12,14] Hence, a new strategy that can harness the benefits of both the conventional coating and doping processes was sought to mitigate the rock-salt phase and residual lithium formation issues at the same time. As mentioned previously, the surface (≈30 nm) was reconstructed via interdiffusion between the coating material and Ni from the high-Ni layered oxide, effectively lowering the Ni concentration at the surface and reducing the amount of residual lithium (Figure 1b). This beneficial surface reconstruction, however, also suggests that the rock-salt phase could also be reduced owing to the decreased Ni concentration at the high-Ni layered oxide surface. Therefore, this study indicated that fostering interdiffusion to reconstruct the surface could serve as a key solution for simultaneously lowering the rock-salt phase and residual lithium, and hence we adopted this surface modification strategy.

2.2. Screening of Suitable Ions for the Coating Precursor of the Interdiffusion-Based Surface Reconstruction via Dry Coating Process

Because of the reliance of the surface modification strategy on the interdiffusion process between the coating material and the high-Ni layered oxide, applying a coating material that can form a solid-solution with the high-Ni layered oxide is a prerequisite. In that regard, the obvious choice for the class of coating materials would be metal hydroxides or oxides. But not all metal hydroxides or oxides can form a solid solution with the high-Ni layered oxide. Thus, our first step for screening the suitable metal ions for the coating material was to identify hydroxides or oxides of which metals can form a solid solution with the high-Ni layered oxide. Possible candidate ions are Na, Mg, Al, Ti, Cr, Mn, Fe, Co, and Ga. Among these candidates, Na, Mg, Cr, Mn, and Ga were excluded. Larger ionic size of Na^+ (1.02 Å) and Mg^{2+} (0.72 Å) can occupy Li sites,[15] and Cr^{3+} is unfavorable under highly oxidative environment.[16] Also, low diffusivity (Mn^{4+})[10c] and solubility (Ga^{3+})[17] in LNO can limit the interdiffusion reaction. Therefore, we further investigated the suitability of the four remaining candidates, Al, Ti, Fe, and Co.

Our second screening step was to explore which ion makes Ni migration to the Li layer in the high-Ni layered oxides unfavorable after the surface reconstruction. As mentioned

© 2021 Wiley-VCH GmbH

earlier, the rock-salt phase that predominantly consists of Ni^{2+} can be formed, and causes a high degree of Li/Ni mixing at surface.[4f,6b,18] To minimize the degree of Li/Ni mixing in high-Ni layered oxides, the theory of superexchange interaction (e.g., Ni^{2+}–O^{2-}–M^{n+}) in the interdiffusion layer (≈30 nm) was considered.[19] Superexchange denotes the magnetic interaction of two neighboring TM cations the share a non-magnetic intermediate anion (e.g., M^{n+}-O^{2-}-M^{n+}). As elucidated in Goodenough-Kanamori-Anderson rules, the sign and strength of this superexchange interaction is highly dependent on the cation-anion-cation bond angle.[20] While a 180° superexchange involves two magnetic cations with partially filled d orbitals forming a strong antiferromagnetic interaction, a 90° superexchange involves one or two non-magnetic cations forming a ferromagnetic interaction that is relatively weaker. In high-Ni layered oxides, the Ni^{2+} (Li layer) –O^{2-}–Ni^{3+} (TM layer) bond, which arises with Ni migration to the lithium layer (Li/Ni mixing,) forms a strong 180° superexchange interaction because both Ni^{2+} and Ni^{3+} have an unpaired electron in the 3d orbitals. Ni^{3+} ions with one unpaired electron in the 3d orbital could also be considered to be present in the Li layer due to superexchange interaction, but Ni^{2+} prefers to occupy Li layer as Ni^{2+} and Li^{+} ions have a smaller difference in size and charge compared to that between Ni^{3+} and Li^{+}. In other words, these interactions would render Ni^{2+} its stability in the lithium layer. In contrast, a 90° superexchange interaction with a non-magnetic cation would not provide that stability for Ni^{2+}. Thus, the key design principle is to form a 90° superexchange interaction by replacing Ni^{3+} in the TM layer with non-magnetic cations to effectively reduce the degree of Li/Ni mixing.

Figure 1c displays a supercell of a typical high-Ni layered oxide with Li/Ni mixing. A small amount of Ni^{2+} occupies the Li site in the Li layer (in red) due to the intrinsic characteristics of the high-Ni layered oxide materials, resulting in forming a 180° Ni^{2+}–O^{2-}–Ni^{3+} coordinated structural unit. In a similar manner, a supercell of the high-Ni layered oxide after surface reconstruction via interdiffusion was modelled and the Ni^{2+} stability in the Li layer was evaluated by comparing the magnetic superexchange interaction stabilization for each of the candidate ions by substituting them at the purple position, as shown in Figure 1d. Considering the high concentration gradient of coating ions in the interdiffusion layer (≈30 nm) after coating on high-Ni layered oxides, the presence of rock-salt phase at the surface with four different coating ions can clearly assess through the theory of superexchange interaction.

As Ni^{2+}, Ni^{3+} and Co^{3+} exhibit a low spin (LS) state, while the Fe^{3+} is in a high spin (HS) state in layered structure, their 3d electronic configurations are, respectively, $t_{2g}{}^{6}d_{z2}{}^{1}d_{x2\text{-}y2}{}^{1}$, $t_{2g}{}^{6}d_{z2}{}^{1}d_{x2\text{-}y2}{}^{0}$, $t_{2g}{}^{6}$, and $t_{2g}{}^{3}d_{z2}{}^{1}d_{x2\text{-}y2}{}^{1}$ (Figure S1, Supporting Information). As can be seen, Ni^{2+}, Ni^{3+} and Fe^{3+} all have at least one unpaired electron in the 3d orbital while Co^{3+} does not. Hence, both Ni^{3+} and Fe^{3+} form a strong 180° superexchange interaction with Ni^{2+} whereas Co^{3+} forms a 90° superexchange interaction with Ni^{2+} (Figure 1e). It indicates that Ni^{2+} would not be stable after Co doping, unlike Fe doping, resulting in the suppression of Li/Ni mixing in the high-Ni layered oxides. In addition, substitution of the other non-magnetic cations, Al^{3+}, and Ti^{4+} into the TM layer in the high-Ni layered oxides are expected to restrict the 180° superexchange interaction as they do not have any electrons in their 3d shell.[12] Therefore, Fe would not be suitable and was ruled out from the candidates of coating ions.

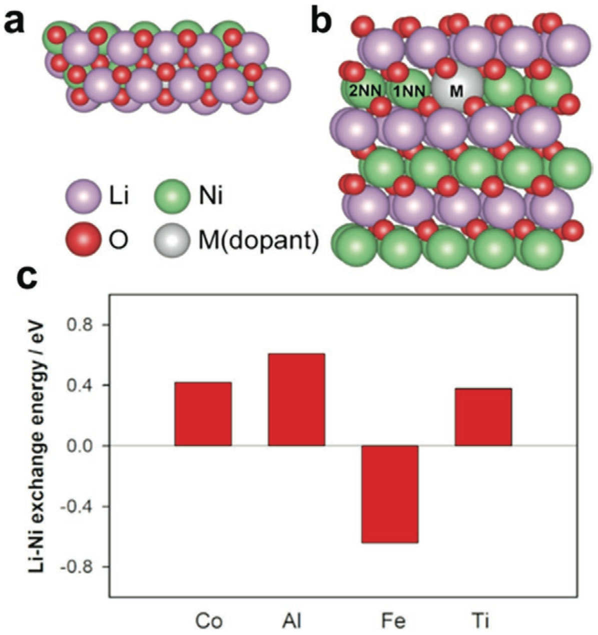

Figure 2. Model of a) top and b) side view and c) the lowest Li-Ni exchange energies of $Li_{30}Ni_{29}M_{1}O_{60}$ (M: Al, Ti, Fe, and Co).

To better understand the effect of suppressing the Li/Ni mixing with four candidates by interdiffusion-based surface reconstruction, the Li/Ni exchange energy with four different dopants in $LiNiO_2$ was investigated with DFT calculations. The model for the bulk $LiNiO_2$ structure contained 30 Li, 30 Ni, and 60 O atoms, as shown in **Figure 2**a,b. The doping was implemented by replacing one Ni site by each of the four dopants in the supercell. We calculated the Li/Ni exchange energy for both one and two Ni atom(s) swapping with Li at the first and second nearest neighbor (1NN and 2NN) sites, as shown in Figure S2 (Supporting Information), with the following equations:

$$\Delta E_{\text{mix}} = E_{\text{afterLi/Nimixing}} - E_{\text{beforeLi/Nimixing}} \tag{4}$$

where $E_{\text{before Li/Ni mixing}}$ and $E_{\text{after Li/Ni mixing}}$ are the total energy of the system before and after Li/Ni mixing. The smallest Li/Ni exchange energies for the four candidate dopants in LNO are shown in Figure 2c. These computational results indicate that Li/Ni mixing of Al-, Ti-, and Co-doped LNO is unfavorable ($\Delta E_{\text{mix}} > 0$), whereas Fe-doped LNO is favorable ($\Delta E_{\text{mix}} < 0$). This means that Fe coating in high-Ni cathodes is expected to increase the degree of Li/Ni mixing as compared to the other candidates, which is further supported by the fact that Fe dopants are inappropriate for inhibiting unwanted surface reconstruction, such as formation of rock-salt phase and residual lithium, in high-Ni cathodes.

Finally, we considered the oxidation state of the coating ions in the high-Ni layered oxides. In a stoichiometric $Li(TM)O_2$ layered structure, the average oxidation state of the TM is 3+. When the oxidation state of a dopant is greater than or equal to 4+, Ni^{3+} can be reduced to Ni^{2+} to maintain charge neutrality.[21]

© 2021 Wiley-VCH GmbH

For Ti, which would be in the structure as Ti^{4+}, its presence would promote the formation of unwanted Ni^{2+},[22] although Ti^{4+} would form a 90° superexchange interaction. Generally, coating ions can be diffused within tens of nanometers. This implies that the local concentration of titanium in the Ti-coated cathode materials at the surface is much higher compared to that in the Ti-doped cathode materials, which can lead to a more severe Li/Ni mixing at the surface. Thus, Ti was also deemed unfavorable and ruled out from the candidates of coating ions. As a result, Al and Co were screened as the suitable metal ions for coating precursors to alleviate the issues of rock-salt phase formation and residual lithium.

2.3. Verification of the Screening Principles and Characterization of the Effect of Interdiffusion-Based Surface Reconstruction via Dry Coating Process on NMC91

Having screened the suitable metal ions for the coating precursors, the rationality of the screening principles was verified by synthesizing and characterizing the dry-coated NMC91. **Figure 3**a,b displays the visualization of NiO$^-$ and LiCO$_3^-$ from the cross-sections of NMC91. The ToF-SIMS mapping represents the fragment distribution of LiCO$_3^-$—the marker for lithium carbonate—illustrating that residual lithium is present at the surface in NMC91. In addition to the metal precursors of Al and Co, those of Ti and Fe were also applied as coating materials in order to determine whether our screening principles were and Ti and Fe as unsuitable coating ions. The NMC91 coated with Al, Ti, Fe, and Co precursors via the dry coating process and annealed in a pure oxygen stream are, respectively, referred to as Al-NMC91, Ti-NMC91, Fe-NMC91, and Co-NMC91. Morphologies of all the samples are also shown in Figure S3 (Supporting Information). The first characteristics analyzed was the residual lithium concentration, which was measured for the pristine NMC91 and the coated NMC91 via an acid-base titration, as shown in Figure 3c. The total residual lithium concentration was 3695 ppm for the pristine NMC91. For all of the coated NMC91 samples, their residual lithium concentration decreased compared to the pristine NMC91. It is noteworthy that the residual lithium decreased in the order Ti-NMC91 (2477 ppm) > Fe-NMC91 (2312 ppm) > Al-NMC91 (1831 ppm) > Co-NMC91 (1459 ppm), which is consistent with our theoretical screening results. For a comparison of the effect between coating and doping, the same amount of the cobalt precursor was added during the NMC91 synthesis step to dope Co into the bulk and the residual lithium concentration of the Co-doped NMC91 was 2625 ppm. This clearly proves that the propitious surface reconstruction strategy can more effectively remove the residual lithium than bulk doping as the doping effect is concentrated at the surface (interdiffusion) rather than being homogenously distributed in the bulk.

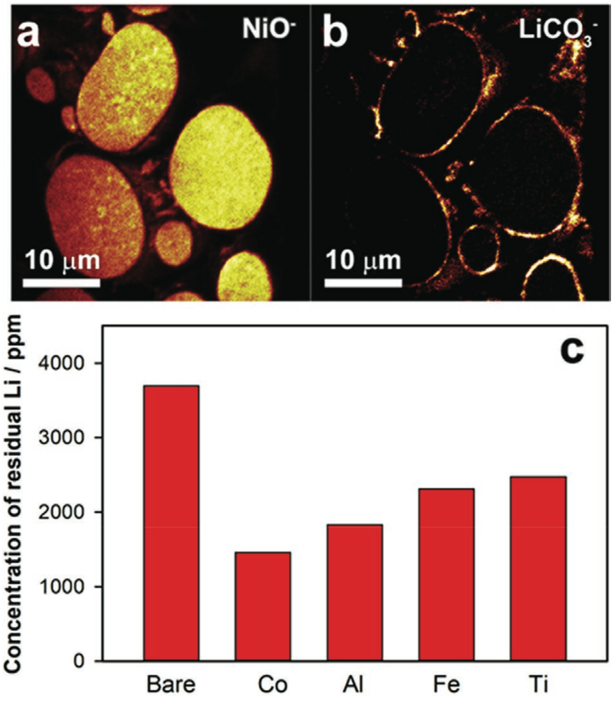

Figure 3. ToF-SIMS cross-sectional chemical mapping for a) NiO$^-$ and b) LiCO3$^-$ secondary ion fragments from NMC91; c) Residual lithium concentrations (ppm) of untreated NMC91 (bare), Al-NMC91 (Al), Ti-NMC91 (Ti), Fe-NMC91 (Fe), and Co-NMC91 (Co).

Also, the degree of Li/Ni mixing follows a similar trend in improvement. Figure S4 and Table S1 (Supporting Information), respectively, show the powder X-ray diffraction (XRD) and the refined patterns of the five samples and a summary of the Rietveld refinement results. The structures of all samples matched well to the hexagonal *α*-NaFeO$_2$ structure (*R-3m*) without any impurity phases. Ti-NMC91 (5.63%) and Fe-NMC91 (4.81%) exhibit higher degrees of Li/Ni mixing compared to the pristine NMC91 (4.40%). This indicates the increased Ni^{2+} content in NMC91 is due to, respectively, the maintenance of charge neutrality with Ti^{4+} introduction and the formation of a strong superexchange interaction between Ni^{2+} and Fe^{3+} (180° Ni^{2+}–O^{2-}–Fe^{3+} superexchange configuration). In contrast, Li/Ni mixing in both Al-NMC91 (3.85%) and Co-NMC91 (3.49%) significantly decreased as the formation of 90° superexchange interaction with Al^{3+} or Co^{3+} would be unfavorable for Ni^{2+}. The results support that fostering Ni^{3+} stability in high-Ni layered oxides by dry coating of Al or Co hydroxide precursors can considerably reduce the residual lithium.

While applying both Al and Co coating materials have significantly reduced the residual lithium concentration in NMC91 as predicted, Co-NMC91 actually exhibited lower residual lithium contents than Al-NMC91. To gain an in-depth understanding of the difference in residual lithium contents between Al and Co, elemental compositions of the surface of Al- and Co-NMC were further investigated with a STEM equipped with energy dispersive spectroscopy (EDS). Figure S5 (Supporting Information) presents the EDS elemental mapping of NMC91, Al-NMC91, and Co-NMC91. The elemental mapping of cobalt in Co-NMC91 clearly shows the high concentration of Co on the plate-shaped nanostructures on the surface (Figures S3b and S5b, Supporting Information), demonstrating the reconstructed surface. In contrast, such surface modification cannot be observed with Al-NMC91, exhibiting little difference in the elemental distributions of Ni, Co, and Mn between the NMC91 and Al-NMC91 (Figures S3a, S3c, S5a and S5c, Supporting Information). In fact, in Al-NMC91, Al is uniformly distributed

© 2021 Wiley-VCH GmbH

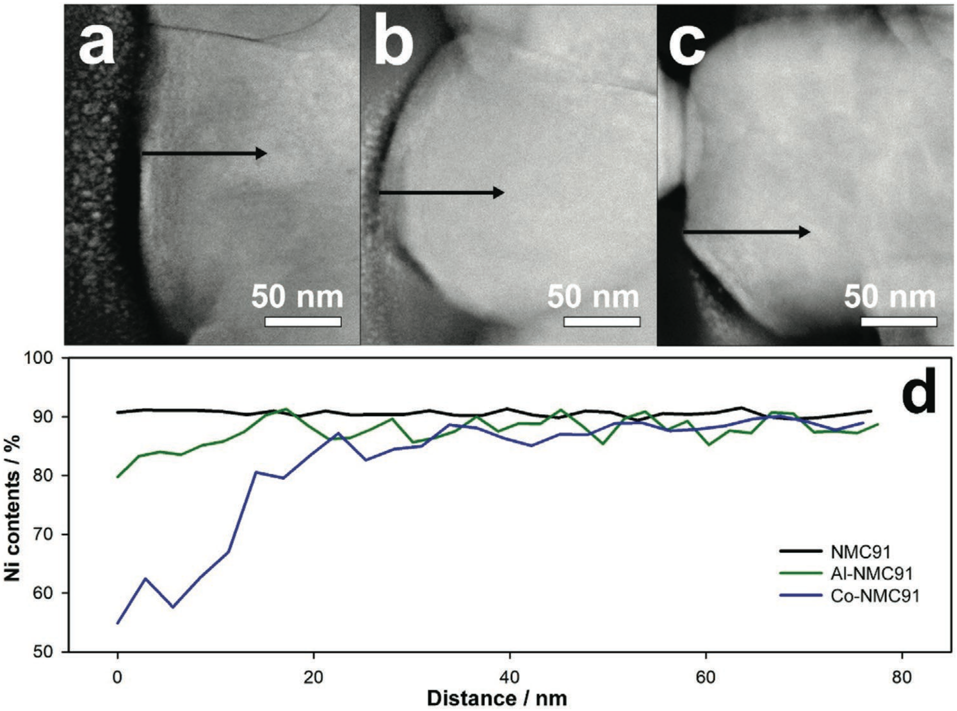

Figure 4. Quantitative elemental analyses on NMC91, Al-NMC91, and Co-NMC91 secondary particles from their surface to the bulk: HR-STEM cross-sectional images of a) NMC91, b) Al-NMC91, and c) Co-NMC91, and d) comparison of the EDS line profile of Ni distribution along their respective black arrows (≈75 nm) in (a–c).

throughout the particle as shown in Figure S5c (Supporting Information), which explains the decrease in the residual lithium concentration in Al-NMC91 but to a lesser extent compared to Co-NMC91. To further verify the compositional changes of NMC91, Al-NMC91, and Co-NMC91, TEM EDS line scans were acquired along the black arrows (from the surface to ≈75 nm into the bulk), as shown in **Figure 4** and Figure S6 (Supporting Information). As expected, the Ni concentration in NMC91 is constant at 91% (Figure 4d). Al-NMC91 also shows a constant Ni concentration at ≈80%, further confirming the bulk diffusion of Al. On the other hand, there is a Ni concentration gradient within the 20 nm of the surface layer in Co-NMC91 with only 55% Ni at the surface. These surface reconstructions result from interdiffusion between coating layer and bulk NMC91.[10c,23] This lower Ni concentration in Co-NMC91 at the surface greatly contributes to suppress the leaching out of lithium, leading to a more effective reduction in the residual lithium than Al-NMC91. These results also show that for the same annealing conditions after the dry coating of the metal precursors, the diffusion of Al^{3+} is more facile than Co^{3+} in the layered structure, resulting in its diffusion into the bulk rather than localization at the surface. This difference in the diffusion rates between Al^{3+} and Co^{3+} in NMC cathode materials is well consistent with a previous study.[23b] This would affect both the surface and bulk properties of NMC91 and, therefore, it is desirable that the coating ions minimize the Ni concentration within 20 nm at the surface through the interdiffusion process.

In addition, high angle annular dark field scanning transmission electron microscopy (HAADF-STEM) images and electron energy loss (EEL) spectra of NMC91 and Co-NMC91 in **Figure 5** obviously revealed reduced rock-salt phase region due to interdiffusion-based surface reconstruction. The Li/Ni mixing in NMC91 is clearly observed compared to Co-NMC91 in the HAADF STEM images, as shown in Figure 5a,b. As crucial information on local structural environment, such as chemical bonding between ligands, spin states, and hybridization of metal ions can be determined, the O K-edge EEL spectra of NMC91 (Figure 5e) and Co-NMC91 (Figure 5f) were collected from the surface to the bulk corresponding to Figure 5c,d. In layered oxides, the O-K pre-edge peak at ≈528 eV and O-K edge peak at ≈540 eV, respectively, correspond to the transition of O 1s electron to the O 2p-TM 3d and O 2p-TM 4sp hybridization states. In other words, the lower intensity means the more the oxygen deficiency and the reduction of TMs (e.g., formation of a rock-salt phase).[24] As shown in Figure 5e, for NMC91 the O-K pre-edge peak intensity is weak at the surface (red), meaning that the surface region is converted to the rock-salt phase, which is in good agreement with numerous studies.[6b,18a,25] With Co-NMC91, the O-K pre-edge peak intensity of the EEL spectrum from the surface (red, Figure 5f) is similar to those of the EEL spectra obtained from the bulk. Moreover, energy loss difference between pre-edge and main edge (ΔE) in O-K edge at their highest intensities provides the information of Ni oxidation state.[24d,e] The increasing or decreasing ΔE represents oxidation or reduction of TM ions bound to oxygen. As shown in Figure 5g, the ΔE of the O-K edge in NMC91 increases from surface to bulk (within ≈10 nm), whereas Co-NMC91 shows little change. This means that Ni oxidation state on the surface is lower than that in the bulk NMC91, and that of Co-NMC91 is almost similar from the surface to bulk. To further investigate

© 2021 Wiley-VCH GmbH

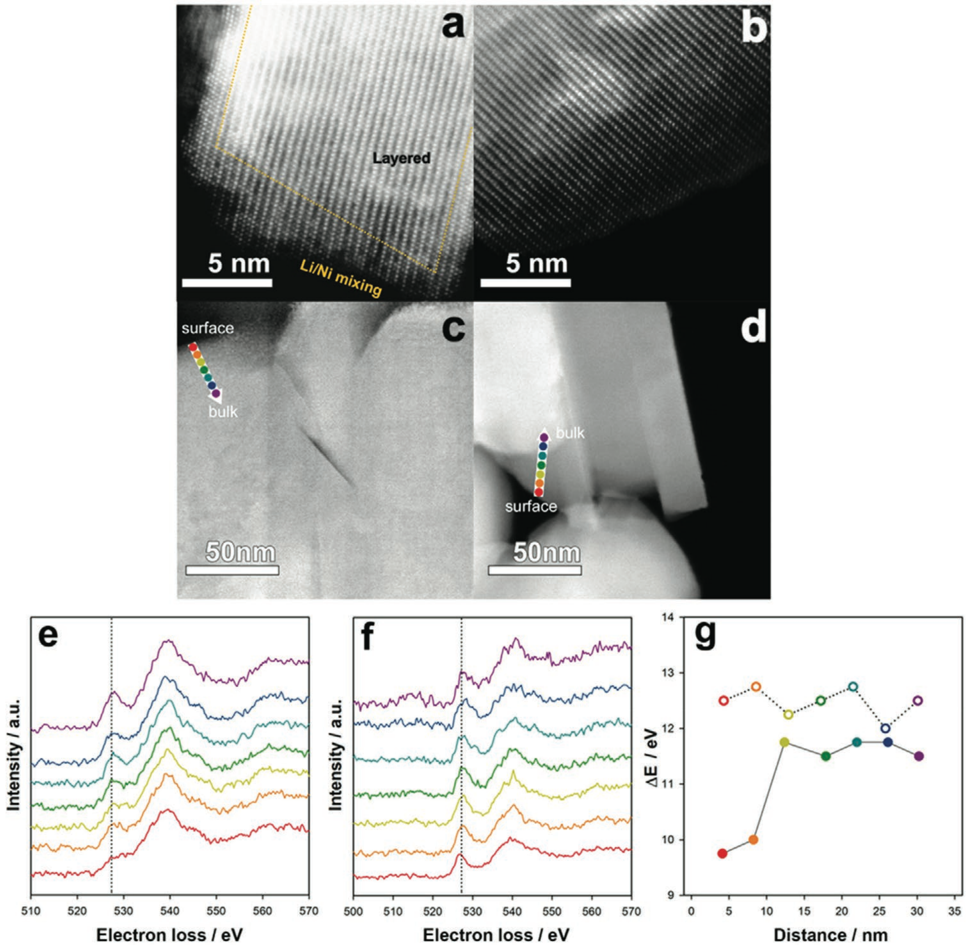

Figure 5. HAADF-STEM images of a,c) NMC91 and b,d) Co-NMC91; EELS O-K edges from the surface to the bulk in e) NMC91 and f) Co-NMC91 (pre-edge: ≈527.5 eV and main edge: ≈540 eV), and g) evolutions in the ΔE of O-K edges of NMC91 and Co-NMC91 from surface to bulk (filled circle: NMC91 and unfilled circle: Co-NMC91).

the change of Ni local environment, Ni-$L_{2,3}$ edges were obtained. Figure S8 (Supporting Information) shows Ni-$L_{2,3}$ edges of NMC91 and Co-NMC91. At the surface of bare NMC91, a significant increase in L_3/L_2 ratio of Ni means that the charge compensation of oxygen ions or the loss of oxygen is induced mostly by the reduction of Ni ions, whereas Co-NMC91 shows little change (Figure S8c, Supporting Information). This trend is consistent with the O k-edge EEL spectra. This confirms that the beneficial surface reconstruction by coating cobalt hydroxide reduces the Ni concentration at the surface which consequently results in the reduction of the rock-salt phase at the surface.

2.4. Electrochemical Performances

The electrochemical performance of the five cathode materials were evaluated with coin half cells paired with lithium metal anode at 30 °C and detailed electrochemical characteristics, as shown in **Figure 6** and Table S2 (Supporting information). During the initial C/10 formation cycle within 3.0–4.35 V (vs Li/Li$^+$), NMC91, Co-NMC91, Al-NMC91, Fe-NMC91, and Ti-NMC91 delivered a discharge capacity of, respectively, 226, 225, 215, 224, and 198 mA h g^{-1} (Figure 6a). The relatively lower initial discharge capacities of Al-NMC91 and Ti-NMC91 are ascribed to larger polarization due to hindered the Li-ion transfer after coating aluminum and titanium oxide on NMC91.[22b,23,26] Figure 6b compares the cycling performance of all the cathode materials at a rate of C/2 within 3.0–4.3 V (vs Li/Li$^+$). After 100 cycles, Al-NMC91 (87%) and Co-NMC91 (87%) show better capacity retention than NMC91 (84%), whereas Ti-NMC91 (78%) and Fe-NMC91 (83%) fare worse. The results illustrate that Co-NMC91 demonstrate superior electrochemical performance over other electrode materials in terms of specific capacity and cycle performance. Coating layer can effectively mitigate unwanted side reaction with electrolyte. The side reaction between residual Li and electrolyte can increases the formation of cathode electrolyte interphase (CEI) layer on the cathode surface during cycling, thus resulting in poor cycle performance.[7a,10a,b] Simultaneously, layered to rock-salt phase transition at the surface on high-Ni cathode material particles due to electrode–electrolyte interaction can lead to decreasing the capacity retention.[27]

To investigate correlation between the coating layer and phase transition after long-term cycling, ex situ XRD analysis

© 2021 Wiley-VCH GmbH

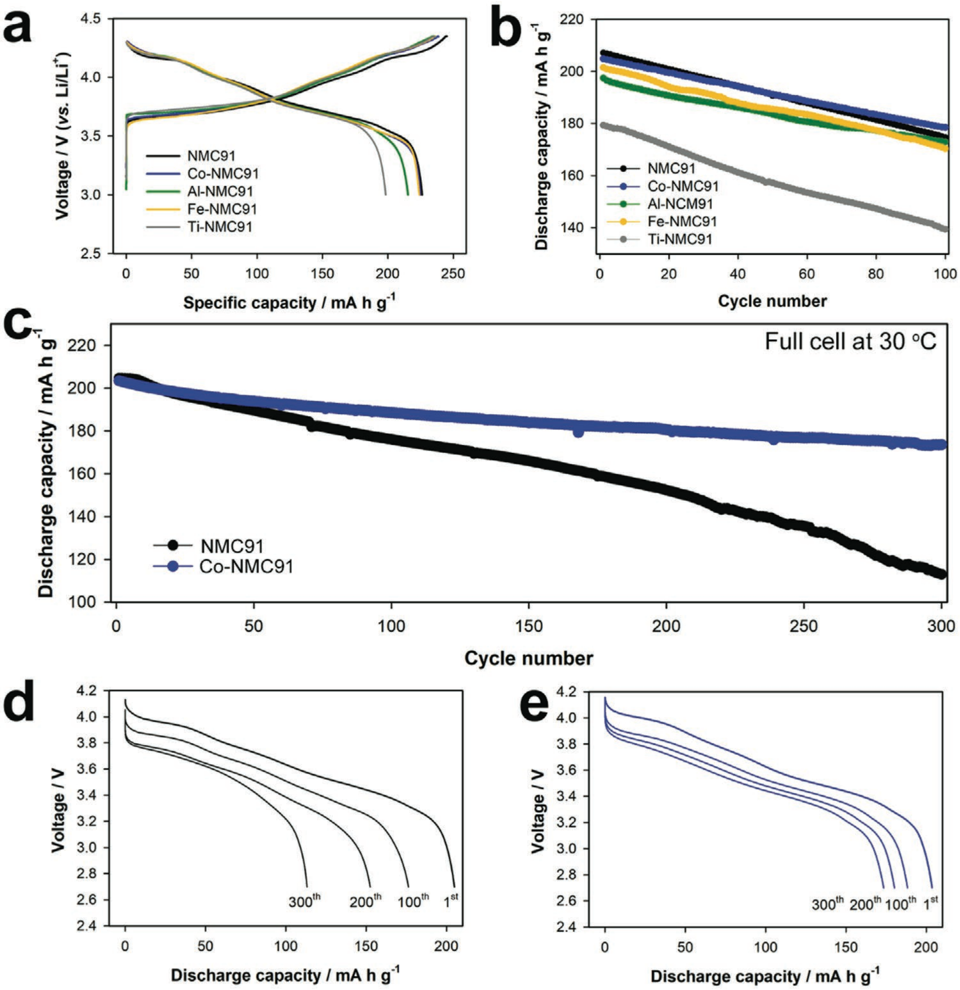

Figure 6. Electrochemical performance of NMC91, Co-NMC91, Al-NMC91, Fe-NMC91, and Ti-NMC91 in coin half-cells at 30 °C: a) voltage profiles of the formation cycles and b) cycle performance at a rate of C/2 within 3.0–4.3 V versus Li, and c) coin full cell cycling performance of NMC91 and Co-NMC91 at 30 °C cycling at a rate of C/2 within 2.7–4.25 V. Evolution of discharge voltage profiles of d) NMC91 and e) Co-NMC91 at the 1st, 100th, 200th, and 300th cycles.

was performed. The peak ratio of $I_{(003)}/I_{(104)}$ in the ex situ XRD pattern indicates the degree of Li/Ni mixing and can be used to determine the layered-to-spinel or rock-salt phase transition in which ratios lower than 1.2 represent significant Li/Ni mixing.[27] The cells of all the cathode materials after 100 cycles were disassembled for ex situ XRD to compare the degree of layered-to-spinel or rock-salt phase transition from surface to bulk, as shown in Figure S9 (Supporting information). The intensity (003) to (104) peak ratio of Al- and Co-NMC91 are higher than 1.2, whereas that of bare, Fe- and Ti-NMC91 are lower than 1.2. This trend is consistent with cycle performance of all the samples. Thus, suppressing phase transition as well as reducing residual lithium in Al- and Co-NMC91 contributed to improve the cycle performances.

To gain further insight into its behavior in an actual cell, the cycle performances of untreated NMC91 and Co-NMC91 were evaluated in a coin full cell set-up at 30 °C. The areal capacity of the full cells was designed to be 2.9 mA h cm^{-2}. Notably, the NMC91 and Co-NMC91 in coin full cells exhibit a significant capacity retention of 56% and 85% after 300 cycles (Figure 6c). Evolution of discharge voltage profiles upon cycling further reflects the polarization between NCM91 (Figure 6d) and Co-NMC91 (Figure 6e). The remarkable long-term and high temperature cycling performance of Co-NMC91 is attributed to the lowering of Ni concentration at the surface by the Co coating that effectively reconstructed the cathode surface to reduce the rock-salt phase and residual lithium species.

3. Conclusion

Herein, we presented a rational strategy of interdiffusion-based advantageous surface reconstruction via dry coating and annealing of a metal-ion precursor to simultaneously address both the issues of rock-salt phase and residual lithium formation on the surface of NMC91 that arise due to the reduction of Ni^{2+} caused by the relative instability of Ni^{3+} at the surface. Thus, decreasing the Ni^{2+} contents at the surface of NMC91 by the coating materials is the key to mitigating the inherent issues. Among the various metal ions, Al and Co were screened

© 2021 Wiley-VCH GmbH

as suitable ions for the coating precursor by considering relevant theoretical aspects. As can be explained by the theory of superexchange interaction and DFT calculations, Ni^{3+} reduction to Ni^{2+} would be unfavored with the non-magnetic Al^{3+} or Co^{3+} ions in the layered structure of NMC91 as that would result in weak 90° superexchange interactions. Also, employing ions with an oxidation state of $< 4+$ is critical to reduce the Ni^{2+} contents. To verify the effectiveness of the strategy and the rationality of the screening process, Al, Ti, Fe, and Co coating on NMC91 was experimentally investigated. Although Ti and Fe coating did reduce the residual lithium content in NMC91, the coating aggravated Ni^{3+} reduction to Ni^{2+} as had been anticipated at the screening stage. While Al and Co reduced both the residual lithium and Ni^{3+} reduction to Ni^{2+}, it was discovered through STEM EELS and EDS study that Co was more effective as its coating led to a lower Ni concentration via surface reconstruction, resulting in a reduction in rock-salt phase and residual lithium. The analyzed characteristics translated to the electrochemical performance, with the Co-coated NMC91 showing the best cycling stability. From a combination of theoretical and experimental studies, Co was successfully identified as the optimum coating ion for the interdiffusion-based surface reconstruction strategy. We expect this study on reducing rock-salt phase and residual lithium formation at the surface of high-Ni layered oxides to open a new avenue for developing high energy density batteries for EV applications.

4. Experimental Section

Materials Synthesis: Spherical $Ni_{0.91}Mn_{0.03}Co_{0.06}(OH)_2$ precursors were obtained by a hydroxide co-precipitation method with a continuously stirred tank reactor (CSTR). Stoichiometric amounts of $NiSO_4 \cdot 6H_2O$, $MnSO_4 \cdot H_2O$, and $CoSO_4 \cdot 7H_2O$ were dissolved in deionized water and stirred to achieve a homogeneous solution. Then, ammonium hydroxide (NH_4OH) and sodium hydroxide (NaOH) solutions, which respectively act as chelation and precipitation agent were added to form co-precipitated $Ni_{0.91}Co_{0.06}Mn_{0.03}(OH)_2$ with stirring. The precursor was thoroughly washed and filtered several times and dried overnight at 180°C. As-prepared precursors were then thoroughly mixed with lithium hydroxide monohydrate (battery grade, Alfa Aesar) before heating under O_2 atmosphere at 670 °C for 10 h (heating and cooling rate: 2 °C min^{-1}). For Co-doped NMC91, 0.04 м $Co(OH)_2$ was mixed with lithium hydroxide monohydrate the prepared coprecipitated hydroxide precursor. For achieving Al-NMC91, Co-NMC91, and Fe-NMC91 via dry coating, the obtained $LiNi_{0.91}Co_{0.06}Mn_{0.03}O_2$ was thoroughly mixed with, respectively, 0.04 molar equivalents of $Al(OH)_3$ (76.5% min, Alfa Aesar), $Co(OH)_2$ (99.9%, Alfa Aesar), and FeOOH (99%, Alfa Aesar). In the case of Ti-NMC91, 0.02 molar equivalent of nano-sized TiO_2 (99.5%, US nano) was mixed with $LiNi_{0.91}Co_{0.06}Mn_{0.03}O_2$, considering formation of Li_2TiO_3. Then, the mixtures were annealed at 720 °C for 6 h in a pure O_2 stream.

Characterization: The total residual lithium concentration in each sample was measured via an acid-base titration with a potentiometric auto titrator (Mettler Toledo, Easy pH Titrator). For preparing the titration samples, 2 g of the synthesized cathode material was dispersed in 100 mL of deionized water for 10 min and then was filtered to obtain the filtrate. Afterward, 80 mL of the filtrate was titrated with 0.1 м hydrochloric acid. The detailed calculation method for residual lithium concentration was discussed in the previous paper.[13] To avoid contamination during storage, the titration was performed on all of the samples directly after synthesis. XRD patterns of the samples were acquired for structural analyses from 10° to 80° with a 0.04° scan step (Rigaku Miniflex 600). Also, Rietveld refinement was performed on the acquired XRD patterns using Fullprof software. The morphology of the samples was observed with a scanning electron microscopy (SEM) with FEI Quanta 650. Cross-sections of the cathode particles were obtained with focused ion beam (FIB, Scios 2HiVac Dual beam FIB, Thermo Fisher Scientific). Transmission electron microscopy was performed using a JEOL NEOARM equipped with a probe corrector for STEM and an EDS. An accelerating voltage of 80 kV was used to minimize damage. The energy loss difference between pre-edge and main edge (ΔE) was also obtained (Figure S7, Supporting Information). ToF-SIMS analysis was performed with a ToF.SIMS 5 spectrometer (ION-TOF GmbH) to understand the chemical composition variation with depth through high lateral resolution mapping. To avoid contamination of all samples, the samples were transferred from the glove box to the ToF-SIMS instrument using an in-house designed air-free setup. For high-resolution mapping, 30 keV Bi^+ ion beam (≈3 pA of measured sample current) was applied for raster scanning over 35 × 35 μm^2 area. The measurements were performed at 10^{-9} Torr base pressure. Cs^+ ion beam sputtering rate has been previously established at ≈0.03 nm s^{-1}.[28]

Computation Method: GGA-level spin-polarized DFT calculations were performed with the Vienna ab initio simulation package using a plane wave basis set with a cut-off of 450 eV. The Perdew-Burke-Ernzerhof functional was used to describe electron exchange and correlation.[29] The DFT+U method was employed to treat localized Ni, Co, Ti, and Fe 3d orbitals with effective U values of 5.9, 3.3, 4.0, and 4.0 eV, respectively.[19c,29–30] The Brillouin zone was sampled with a $3 \times 6 \times 3$ k-point mesh following the Monkhorst-Pack scheme. The convergence criteria for electronic and geometrical optimization were 10^{-5} eV and 10^{-2} eV Å^{-1}, respectively. All the systems in this work were layered structure with the space group *R-3m* and expanded to $3 \times 1 \times 1$ supercell (Figure 2a,b).

Electrochemical Tests: A typical cathode was prepared by first mixing the electrode material, carbon black (Super P), and poly(vinylidene fluoride) (PVdF) at mass ratio of 90:5:5 (for half-cell) and 92:4:4 (for full-cell) in *N*-methyl-2-pyrrolidone (NMP, 99%, Sigma-Aldrich) solvent to obtain a slurry. The slurry was then casted onto an Al current collector before drying in a vacuum oven. The anode was prepared by mixing graphite, carboxymethyl cellulose (CMC) and styrene-butadiene rubber with a mass ratio of 97.5:1:1.5. For coin half cells, the mass loading of cathodes was ≈5 mg cm^{-2}. For coin full -cells, cathodes and anodes satisfying an N/P ratio range of 1.05–1.10 (based on the practical graphite capacity of around 2.9 mA h cm^{-2}) were paired. All the electrodes were dried at 120 °C in a vacuum oven overnight. The electrolyte was 1 м $LiPF_6$ in ethylene carbonate (EC)/ethyl methyl carbonate (EMC) (weight ratio = 3:7) with 2 wt% vinylene carbonate (VC) additive. All the cells were cycled with a constant current–constant voltage charging mode (cut-off when the current equivalent to C/20 is reached). For the formation cycle of half-cells, all the cathodes were cycled between 3 and 4.35 V (vs Li/Li^+) at C/10 rate for 3 cycles, followed by 100 cycles at C/2 rate between 3 and 4.3 V (vs Li/Li^+) at 30 °C. The full-cell cycling performance was evaluated between 2.7 and 4.25 V at a current rate of C/20 for 3 cycles at 30 °C, followed by a C/2 rate cycling for 300 cycles (1C = 180 mA g^{-1}) at 30 °C.

Supporting Information

Supporting Information is available from the Wiley Online Library or from the author.

Acknowledgements

The financial support by Samsung SDI is gratefully acknowledged.

Conflict of Interest

A.M. is a co-founder of TexPower, a company focusing on cobalt-free cathode materials for lithium-based batteries.

© 2021 Wiley-VCH GmbH

Data Availability Statement

Data available on request from the authors

Keywords

high-nickel layered oxides, interdiffusion, lithium-ion batteries, residual lithium, rock-salts

Received: April 7, 2021
Revised: August 8, 2021
Published online:

[1] a) A. Manthiram, *Nat. Commun.* **2020**, *11*, 1550; b) J. Kim, H. Lee, H. Cha, M. Yoon, M. Park, J. Cho, *Adv. Energy Mater.* **2018**, *8*, 1702028.

[2] a) W. Li, E. M. Erickson, A. Manthiram, *Nat. Energy* **2020**, *5*, 26; b) Y. Kim, W. M. Seong, A. Manthiram, *Energy Storage Mater.* **2021**, *34*, 250.

[3] a) G. Liu, N. Xu, Y. Zou, K. Zhou, X. Yang, T. Jiao, W. Yang, Y. Yang, J. Zheng, *ACS Appl. Mater. Interfaces* **2021**, *13*, 12069; b) W. Li, X. Liu, H. Celio, P. Smith, A. Dolocan, M. Chi, A. Manthiram, *Adv. Energy Mater.* **2018**, *8*, 1703154; c) S. Klein, P. Harte, J. Henschel, P. Bärmann, K. Borzutzki, T. Beuse, S. van Wickeren, B. Heidrich, J. Kasnatscheew, S. Nowak, M. Winter, T. Placke, *Adv. Energy Mater.* **2021**, *11*, 2003756; d) Y. Zou, K. Zhou, G. Liu, N. Xu, X. Zhang, Y. Yang, J. Zhang, J. Zheng, *ACS Appl. Mater. Interfaces* 16427, **2021**, 13; e) S. Klein, S. van Wickeren, S. Röser, P. Bärmann, K. Borzutzki, B. Heidrich, M. Börner, M. Winter, T. Placke, J. Kasnatscheew, *Adv. Energy Mater.* **2021**, *11*, 2003738.

[4] a) M. Bianchini, M. Roca-Ayats, P. Hartmann, T. Brezesinski, J. Janek, *Angew. Chem., Int. Ed.* **2019**, *58*, 10434; b) M. Bianchini, F. Fauth, P. Hartmann, T. Brezesinski, J. Janek, *J. Mater. Chem. A* **2020**, *8*, 1808; c) S. Ahmed, M. Bianchini, A. Pokle, M. S. Munde, P. Hartmann, T. Brezesinski, A. Beyer, J. Janek, K. Volz, *Adv. Energy Mater.* **2020**, *10*, 2001026; d) S. Kalluri, H. Cha, J. Kim, H. Lee, H. Jang, J. Cho, *Adv. Sci.* **2020**, *7*, 1902844; e) S. Muto, Y. Sasano, K. Tatsumi, T. Sasaki, K. Horibuchi, Y. Takeuchi, Y. Ukyo, *J. Electrochem. Soc.* **2009**, *156*, A371; f) H. Zhang, B. M. May, J. Serrano-Sevillano, M. Casas-Cabanas, J. Cabana, C. Wang, G. Zhou, *Chem. Mater.* **2018**, *30*, 692; g) X. Ren, L. Zou, S. Jiao, D. Mei, M. H. Engelhard, Q. Li, H. Lee, C. Niu, B. D. Adams, C. Wang, J. Liu, J.-G. Zhang, W. Xu, *ACS Energy Lett.* **2019**, *4*, 896.

[5] a) D. Pritzl, T. Teufl, A. T. S. Freiberg, B. Strehle, J. Sicklinger, H. Sommer, P. Hartmann, H. A. Gasteiger, *J. Electrochem. Soc.* **2019**, *166*, A4056; b) H. S. Liu, Z. R. Zhang, Z. L. Gong, Y. Yang, *Electrochem. Solid-State Lett.* **2004**, *7*, A190; c) X. Xiong, Z. Wang, P. Yue, H. Guo, F. Wu, J. Wang, X. Li, *J. Power Sources* **2013**, *222*, 318.

[6] a) S.-K. Jung, H. Gwon, J. Hong, K.-Y. Park, D.-H. Seo, H. Kim, J. Hyun, W. Yang, K. Kang, *Adv. Energy Mater.* **2014**, *4*, 1300787; b) Y. Xia, J. Zheng, C. Wang, M. Gu, *Nano Energy* **2018**, *49*, 434; c) S. Hwang, S. M. Kim, S.-M. Bak, K. Y. Chung, W. Chang, *Chem. Mater.* **2015**, *27*, 6044; d) H.-H. Sun, A. Manthiram, *Chem. Mater.* **2017**, *29*, 8486; e) H. Zhang, F. Omenya, P. Yan, L. Luo, M. S. Whittingham, C. Wang, G. Zhou, *ACS Energy Lett.* **2017**, *2*, 2607.

[7] a) S. W. Doo, S. Lee, H. Kim, J. H. Choi, K. T. Lee, *ACS Appl. Energy Mater.* **2019**, *2*, 6246; b) K. Min, K. Park, S. Y. Park, S.-W. Seo, B. Choi, E. Cho, *J. Electrochem. Soc.* **2018**, *165*, A79; c) Y. You, H. Celio, J. Li, A. Dolocan, A. Manthiram, *Angew. Chem., Int. Ed.* **2018**, *57*, 6480.

[8] a) W. M. Seong, K.-H. Cho, J.-W. Park, H. Park, D. Eum, M. H. Lee, I.-s. S. Kim, J. Lim, K. Kang, *Angew. Chem., Int. Ed.* **2020**, *59*, 18662; b) A. T. S. Freiberg, J. Sicklinger, S. Solchenbach, H. A. Gasteiger, *Electrochim. Acta* **2020**, *346*, 136271; c) S. S. Zhang, X. Fan, C. Wang, *ChemElectroChem* **2019**, *6*, 1536; d) Y. Kim, *J. Mater. Sci.* **2013**, *48*, 8547; e) K. Park, D. J. Ham, S. Y. Park, J. Jang, D.-H. Yeon, S. Moon, S. J. Ahn, *RSC Adv.* **2020**, *10*, 26756.

[9] a) J. Cho, *Electrochem. Commun.* **2003**, *5*, 146; b) K. T. Lee, S. Jeong, J. Cho, *Acc. Chem. Res.* **2013**, *46*, 1161; c) J. Cho, *Solid State Ionics* **2003**, *160*, 241; d) A. M. Kannan, L. Rabenberg, A. Manthiram, *Electrochem. Solid-State Lett.* **2003**, *6*, A16; e) B. Song, W. Li, S.-M. Oh, A. Manthiram, *ACS Appl. Mater. Interfaces* **2017**, *9*, 9718; f) P. Oh, B. Song, W. Li, A. Manthiram, *J. Mater. Chem. A* **2016**, *4*, 5839.

[10] a) J. Kim, H. Ma, H. Cha, H. Lee, J. Sung, M. Seo, P. Oh, M. Park, J. Cho, *Energy Environ. Sci.* **2018**, *11*, 1449; b) J. Kim, J. Lee, H. Ma, H. Y. Jeong, H. Cha, H. Lee, Y. Yoo, M. Park, J. Cho, *Adv. Mater.* **2018**, *30*, 1704309; c) J. Li, R. Doig, J. Camardese, K. Plucknett, J. R. Dahn, *Chem. Mater.* **2015**, *27*, 7765.

[11] G. Dutta, A. Manthiram, J. B. Goodenough, J. C. Grenier, *J. Solid State Chem.* **1992**, *96*, 123.

[12] H. Chen, J. A. Dawson, J. H. Harding, *J. Mater. Chem. A* **2014**, *2*, 7988.

[13] W. M. Seong, Y. Kim, A. Manthiram, *Chem. Mater.* **2020**, *32*, 9479.

[14] a) J. Zhao, W. Zhang, A. Huq, S. T. Misture, B. Zhang, S. Guo, L. Wu, Y. Zhu, Z. Chen, K. Amine, F. Pan, J. Bai, F. Wang, *Adv. Energy Mater.* **2017**, *7*, 1601266; b) M. Jeong, H. Kim, W. Lee, S.-J. Ahn, E. Lee, W.-S. Yoon, *J. Power Sources* **2020**, *474*, 228592.

[15] a) H. Kim, A. Choi, S. W. Doo, J. Lim, Y. Kim, K. T. Lee, *J. Electrochem. Soc.* **2018**, *165*, A201; b) C. Pouillerie, L. Croguennec, P. Biensan, P. Willmann, C. Delmas, *J. Electrochem. Soc.* **2000**, *147*, 2061.

[16] S. Komaba, C. Takei, T. Nakayama, A. Ogata, N. Yabuuchi, *Electrochem. Commun.* **2010**, *12*, 355.

[17] Y. Nishida, K. Nakane, T. Satoh, *J. Power Sources* **1997**, *68*, 561.

[18] a) J. Zhu, S. Sharifi-Asl, J. C. Garcia, H. H. Iddir, J. R. Croy, R. Shahbazian-Yassar, G. Chen, *ACS Appl. Energy Mater.* **2020**, *3*, 4799; b) J. Yang, Y. Xia, *J. Electrochem. Soc.* **2016**, *163*, A2665.

[19] a) M. Li, J. Lu, *Science* **2020**, *367*, 979; b) D. Wang, C. Xin, M. Zhang, J. Bai, J. Zheng, R. Kou, J. Y. Peter Ko, A. Huq, G. Zhong, C.-J. Sun, Y. Yang, Z. Chen, Y. Xiao, K. Amine, F. Pan, F. Wang, *Chem. Mater.* **2019**, *31*, 2731; c) J. Zheng, G. Teng, C. Xin, Z. Zhuo, J. Liu, Q. Li, Z. Hu, M. Xu, S. Yan, W. Yang, F. Pan, *J. Phys. Chem. Lett.* **2017**, *8*, 5537; d) N. A. Chernova, M. Ma, J. Xiao, M. S. Whittingham, J. Breger, C. P. Grey, *Chem. Mater.* **2007**, *19*, 4682.

[20] a) J. Kanamori, *Prog. Theor. Phys.* **1957**, *17*, 177; b) J. B. Goodenough, *Phys. Rev.* **1955**, *100*, 564; c) P. W. Anderson, *Phys. Rev.* **1950**, *79*, 350.

[21] F. Wu, N. Liu, L. Chen, Y. Su, G. Tan, L. Bao, Q. Zhang, Y. Lu, J. Wang, S. Chen, J. Tan, *Nano Energy* **2019**, *59*, 50.

[22] a) L. Croguennec, E. Suard, P. Willmann, C. Delmas, *Chem. Mater.* **2002**, *14*, 2149; b) D. Liu, S. Liu, C. Zhang, L. You, T. Huang, A. Yu, *ACS Sustainable Chem. Eng.* **2019**, *7*, 10661; c) J. Kim, K. Amine, *Electrochem. Commun.* **2001**, *3*, 52.

[23] a) B. Han, T. Paulauskas, B. Key, C. Peebles, J. S. Park, R. F. Klie, J. T. Vaughey, F. Dogan, *ACS Appl. Mater. Interfaces* **2017**, *9*, 14769; b) B. Han, B. Key, S. H. Lapidus, J. C. Garcia, H. Iddir, J. T. Vaughey, F. Dogan, *ACS Appl. Mater. Interfaces* **2017**, *9*, 41291.

[24] a) F. Frati, M. O. J. Y. Hunault, F. M. F. de Groot, *Chem. Rev.* **2020**, *120*, 4056; b) F. Lin, I. M. Markus, M. M. Doeff, H. L. Xin, *Sci. Rep.* **2014**, *4*, 5694; c) W.-S. Yoon, M. Balasubramanian, K. Y. Chung, X.-Q. Yang, J. McBreen, C. P. Grey, D. A. Fischer, *J. Am. Chem. Soc.* **2005**, *127*, 17479; d) E. Jo, J.-H. Park, J. Park, J. Hwang, K. Y. Chung, K.-W. Nam, S. M. Kim, W. Chang, *Nano Energy* **2020**, *78*, 105367; e) E. Jo, S. Hwang, S. M. Kim, W. Chang, *Chem. Mater.* **2017**, *29*,

© 2021 Wiley-VCH GmbH

2708; f) S. Hwang, W. Chang, S. M. Kim, D. Su, D. H. Kim, J. Y. Lee, K. Y. Chung, E. A. Stach, *Chem. Mater.* **2014**, *26*, 1084.

[25] a) Q. Xie, W. Li, A. Dolocan, A. Manthiram, *Chem. Mater.* **2019**, *31*, 8886; b) H. Zhang, B. M. May, F. Omenya, M. S. Whittingham, J. Cabana, G. Zhou, *Chem. Mater.* **2019**, *31*, 7790.

[26] W. Li, S. Lee, A. Manthiram, *Adv. Mater.* **2020**, *32*, 2002718.

[27] a) F. Zhang, S. Lou, S. Li, Z. Yu, Q. Liu, A. Dai, C. Cao, M. F. Toney, M. Ge, X. Xiao, W.-K. Lee, Y. Yao, J. Deng, T. Liu, Y. Tang, G. Yin, J. Lu, D. Su, J. Wang, *Nat. Commun.* **2020**, *11*, 3050; b) A. Mesnier, A. Manthiram, *ACS Appl. Mater. Interfaces* **2020**, *12*, 52826; c) Y. Cho, P. Oh, J. Cho, *Nano Lett.* **2013**, *13*, 1145.

[28] W. Li, A. Dolocan, P. Oh, H. Celio, S. Park, J. Cho, A. Manthiram, *Nat. Commun.* **2017**, *8*, 14589.

[29] a) J. P. Perdew, K. Burke, M. Ernzerhof, *Phys. Rev. Lett.* **1996**, *77*, 3865; b) Y. Zhang, W. Yang, *Phys. Rev. Lett.* **1998**, *80*, 890.

[30] a) L. Wang, T. Maxisch, G. Ceder, *Phys. Rev. B* **2006**, *73*, 195107; b) F. Kong, C. Liang, R. C. Longo, Y. Zheng, K. Cho, *J. Power Sources* **2018**, *378*, 750.

© 2021 Wiley-VCH GmbH